Dense Arrays of Uniform Submicron Pores in Silicon and their Applications

Daniel Brodoceanu, Roey Elnathan, Beatriz Prieto-Simón, Bahman Delalat, Taryn M. Guinan, Elmar Karsten Kroner, Nicolas H. Voelcker, and Tobias Kraus

ACS Applied Materials & Interfaces 7(2)

Keywords:
porous silicon, SALDI substrates, antireflective surfaces, colloidal lithography, metal-assisted chemical etching, polymer fibre arrays

Dense Arrays of Uniform Submicron Pores in Silicon and their Applications

Daniel Brodoceanu,[1‡] Roey Elnathan,[2‡] Beatriz Prieto-Simón,[2] Bahman Delalat,[2] Taryn Guinan,[2] Elmar Kroner,[1] Nicolas H. Voelcker[2] and Tobias Kraus[1]**

[1]INM–Leibniz Institute for New Materials, Campus D2 2, 66123, Saarbruecken, Germany

[2]ARC Centre of Excellence in Convergent Bio-Nano Science and Technology, Mawson Institute, University of South Australia, Adelaide, SA 5001, Australia

ABSTRACT: We report a versatile particle-based route to dense arrays of parallel submicron pores with high aspect ratio in silicon, and explore the application of these arrays in sensors, optics, and polymer micropatterning. Polystyrene (PS) spheres are convectively assembled on gold-coated silicon wafers and sputter-etched, resulting in well-defined gold disc arrays with excellent long-range order. The gold discs act as catalysts in Metal-Assisted Chemical Etching (MACE), yielding uniform pores with straight walls, flat bottoms and high aspect ratio. The resulting pore arrays can be used as robust antireflective surfaces, in biosensing applications, and as templates for polymer replica molding.

KEYWORDS: porous silicon, SALDI substrates, antireflective surfaces, colloidal lithography, metal-assisted chemical etching, polymer fibre arrays

1. INTRODUCTION

Single-crystal silicon is so strong that even densely packed submicron pores with nanometer walls are robust enough to handle manually. Vertically aligned pores can decrease unwanted reflection in solar cells[1,2] and enhance the efficiency of Li-ion batteries[3,4] and biosensors.[5] They can be replicated by polymer molding,[6] or imprinted into metals.[7] Here, we fabricate silicon pore arrays that are suitable for applications that require high densities: sensors where only interfaces contribute to the signal, polymer adhesion management surfaces, and anti-reflective layers.

Ordered porous silicon can be produced by transferring a primary structure from photolithography,[8,9] nanoimprint[10] or colloidal lithography,[11,12] laser interference lithography[13] or block copolymer lithography[14] into an underlying substrate. Reactive Ion Etching (RIE) converts the 2D pattern into three-dimensional pores, but depends on the availability of RIE equipment and is costly. Electrochemical etching is another powerful method for producing dense arrays of high aspect ratio pores in silicon. It is, however, limited to n-type silicon and backside illumination, and one can not control pore diameters over a wide range. Colloidal lithography is a simple alternative based on readily available polymer nanoparticles and can be performed in every wet lab. We combine colloidal lithography with metal-assisted chemical etching (MACE)[2,15] to fabricate dense arrays of pores in silicon. MACE relies on the local catalytic etching activity of a thin layer of noble metal (often silver or gold) deposited on silicon. The noble metal acts as a cathode, causing silicon oxidation and subsequent dissolution in hydrofluoric acid (HF). Patterns in continuous metal thin film are vertically transferred into the silicon substrate: a perforated silver film, for example, forms vertically aligned silicon nanowires (SiNWs) with high aspect ratio (>25).[16] Such high aspect ratio of the nanowires can be achieved

by MACE due to the inherent mechanical stability of the perforated metal layer. On the other hand, non-contiguous metal structures (i.e. isolated particles) tend to move laterally during MACE process, resulting in pores with random orientations.[17,18] Here, we present an approach based on dense arrays of metal discs with smooth edges that yield straight submicron pores in silicon, with flat bottoms and high aspect ratios (Γ~5). Our pore arrays are suitable for applications that require high uniformity, large void fractions and regularity. This includes sensing where the specific active area limits detection: surface-assisted laser desorption/ionization mass spectroscopy (SALDI-MS), electrochemical impedance spectroscopy (EIS), and interferometric Fabry-Pérot refractometry. We show below that all of them profit from dense, straight pores. Antireflective layers require pores with sufficient aspect ratios and diameters below the wavelength of visible light that we created using smaller particles in our process. We also explored unconventional applications accessible with these new substrates. Parallel enzymatic reactions were performed using each pore as a "nanoreactor" in which the gold disc anchors proteins. Finally, very dense polymer fibre arrays were fabricated by molding and tested for their adhesive properties.

2. EXPERIMENTAL SECTION

Preparation of the submicron pore arrays. Colloidal suspension of monodisperse polystyrene (PS) microspheres with diameters of 250 nm, 520 nm, 1 μm and 3.2 μm were acquired from BangsLabs, USA. The Si substrates (<100> p-type, resistivity 5–30 mOhm cm) were ultrasonicated in isopropanol, (Sigma-Aldrich, Germany), then washed with deionized water (Millipore) and dried with nitrogen. Thin films of gold with thickness in the range of 30-50 nm were deposited using a standard DC magnetron sputtering system (JEOL, JFC-1300, Japan) with

argon pressure of 0.08 mbar and 20 mA discharge current, while the distance between metal target and sample was set to 5 cm. In order to render the metal surface hydrophilic necessary for PS monolayer assembly, the gold-coated substrates were treated for 30 s in oxygen plasma (low-pressure reactor PICO, RF source at 13.56 MHz, Diener electronic, Germany) at 0.3 mbar with RF power set to 50 W. Hexagonally close-packed PS monolayers were deposited over approximately 4 square cm by convective assembly using a setup described elsewhere.[19] The gold-coated silicon samples with the PS monolayer assembled on top was fixed on a 2 inch copper disc holder using carbon tape. The copper holder was then mounted on the DC sputter head (cathode), acting as a target for the kinetic argon ions. The chamber was pumped down to about 0.1 mbar and flushed with argon to better remove the adsorbed gas contaminants. When the argon gas reached the operation pressure (0.08 mbar), the sputtering process started at a discharge current of 20 mA and time duration between 20 and 100 s depending on the original PS particle size. The partially etched PS particles were either peeled off using an adhesive tape or dissolved in an organic solvent such as toluene or chloroform. The surface area covered by the metal disc array was estimated using the ImageJ software. The MACE process was carried out at room temperature by immersing the disc array patterned silicon sample for 2 - 30 min in a Teflon beaker containing an etching mixture of deionized water, HF (this chemical requires special safety precautions) and H_2O_2 with concentrations 4.6 M and 0.44 M, respectively. The beaker was knocked at regular interval (once every minute) to remove the hydrogen bubbles generated on the silicon sample during MACE process, as they may negatively impact the pores' etching orientation. After etching, the samples were thoroughly washed with deionised water and dried with nitrogen. SEM images were acquired using an FEI Quanta 400F scanning electron microscope (FEI Europe, Eindhoven).

SALDI-MS: Sample preparation and analysis. Standard solutions of methadone (1 mg/mL) were kindly provided by Forensic Science South Australia (SA, Australia). Stock solutions of methadone (0.1 mg/mL, 1 mL) were prepared from methadone standards and stored at -20^{o}C. Working solutions at 1000 ng/mL were obtained by diluting the stock solutions with MilliQ water. Working solutions were kept at +4^{o}C and were prepared fresh every two weeks. Aliquots of drug solutions (0.5 μL) were deposited onto the silicon pore array. The solvent was allowed to completely evaporate. Upon evaporation, the pore arrays were mounted on a modified MALDI target plate (MTP384, BrukerDaltonics, Bremen, Germany) and analysed. Mass spectra were collected using an Autoflex Series III Bruker MALDI-TOF-TOF mass spectrometer equipped with a SmartBeam (337 nm, Nd:YAG) operated at a pulse frequency of 200 Hz, laser attenuator offset of 22 % in reflectron positive (RP) mode. Mass spectra were generated by averaging 500 individual laser shots. Data acquisition used flexControl3.3 (build 85) software and data analysis was performed using flexAnalysis version 3.3. The parameters for the RP acquisition were set as follows: 19.00 and 16.80 kV for the ion source 1 and 2, respectively, 8.25 kV for the lens and 21.00 and 9.40 kV for reflector 1 and 2, respectively. Quadratic external calibration of the TOF tube was performed before each acquisition on the monoisotopic masses of α-cyano-4-hydroxycinnamic acid (CHCA) adducts, namely CHCA$[M+H-H_2O]^+$, CHCA$[M+H]^+$, CHCA$[M+Na]^+$, CHCA$[2M+H-CO_2]^+$, CHCA$[2M+H]^+$ and CHCA$[3M+Na_2]^+$.

EIS measurements. Silicon substrates with gold discs were cleaned by exposure to Piranha solution (70% concentrated sulfuric acid, 30% hydrogen peroxide) for 30 min. Then, they were rinsed thoroughly with deionized water. Clean gold discs were exposed overnight to a 2 mM mercaptopropionic acid aqueous solution. After rinsing thoroughly with deionized water, the substrates were attached onto copper plates using silver paste to prepare the electrodes. Further

modification steps of the electrode surface were electrochemically characterized by EIS. The measurements were performed with an electrochemical analyser (CH Instruments, model 600D series) using a three-electrode electrochemical cell, placed into a Faraday cage. A pore array-based working electrode (3 mm diameter), a platinum wire counter electrode and a Ag/AgCl reference electrode were fitted in a flow cell. Data acquisition and analysis were accomplished using CH Instruments software (CH Instruments, Inc., Austin, TX, USA). MS2 antibody immobilization was performed by filling the cell with a 1:1 mixture of 10 mg/mL EDC and 15 mg/mL NHS in 0.1 M MES buffer, pH 5.5. After 30 min, the activated surface was incubated with 20 μg/mL MS2 antibody for 1 h at room temperature to form stable amide bonds. The residual active groups were blocked by reaction with 1M ethanolamine-HCl, pH 8.5, for 20 min. Subsequently, 1h incubations of MS2 bacteriophage solutions in a wide range of concentrations (from 1 to 10^{10} pfu/mL) were carried out, followed by non-faradaic EIS measurements. The impedance spectra recorded after incubation of the antibody-modified pore array were fitted to the equivalent circuit model that includes three capacitors in series: the dielectric layer of the insulation (mercaptopropionic acid), the dielectric layer of the receptor layer (antibody), and the double-layer capacitance. In non-faradaic sensors, capacitance (C) is the circuit element commonly used to follow affinity binding. It detects a combination of the surface modification capacitance and the double layer capacitance. Bode plots (log(Z) vs. log(freq)) enable the calculation of the ohmic resistance of the solution (R_s) and the polarization or charge-transfer resistance (R_{ct}). Moreover, at intermediate frequencies those plots can be correlated to a straight line that if extrapolated to the log(freq) axis at freq=1 (thus, log(freq)=0) yields the value of capacitance (C) from the relationship: Z=1/C. Fitting of the Nyquist plots to the equivalent circuit was used to assess changes in charge-transfer resistance (R_{ct}), showing an acceptable error

value ($\chi^2 < 0.05$). To allow comparison of the MS2 antibody-modified pore array and the controls prepared with BSA, all R_{ct} values were normalized as follows: $(R_{ct}^{f}-R_{ct}^{0}))/R_{ct}^{0}$, where R_{ct}^{0} and R_{ct}^{f} are R_{ct} values prior and after bacteriophage interaction.

Enzyme nanoreactors. To immobilize the horseradish peroxidase (HRP) onto the gold discs at the base of the pores, the pore arrays were cleaned by exposure to Piranha solution (70% concentrated sulfuric acid, 30% hydrogen peroxide) for 30 min. They were subsequently rinsed thoroughly with deionized water. The arrays with clean gold discs were exposed overnight to a 2 mM mercaptopropionic acid aqueous solution. After rinsing thoroughly with deionized water, the arrays were incubated with a 1:1 mixture of 10 mg/mL EDC and 15 mg/mL NHS in 0.1 M MES buffer, pH 5.5. After 30 min, the arrays were incubated with 50 µg/mL HRP (Sigma) for 30 min at room temperature to form stable amide bonds. The residual active groups were blocked by reaction with 1 M ethanolamine-HCl, pH 8.5, for 10 min. Afterwards the substrates were washed 3 times with the reaction buffer. In order to detect the enzymatic activity within the pores, a 10 mM stock solution of Ampliflu red (Sigma) was prepared by dissolving 5 mg of Ampliflu red in 1950 µl dimethyl sulfoxide (DMSO). (Stock solution was kept at 4°C in the dark). The reaction buffer comprised of 0.05M sodium phosphate (pH 7.4). A 10 µM H_2O_2 working solution was prepared using reaction buffer as the diluent. An enzymatic reaction was initiated by incubating the working solution with 5 µl of 10 mM Ampliflu red solution for 60 s inside the pores. The fluorescent resorufin generated in the pores was detected using a Nikon Eclipse TiS inverted fluorescence microscope.

Optical reflectivity measurements. White light from a tungsten lamp (Ocean Optics) was fed through one end of a bifurcated fibre-optic cable and focused through a lens onto the pore array in silicon at normal incidence with a spot size of approximately 1 mm in diameter. Light

reflected from the array was collected through the same optics, and the distal end of the bifurcated fibre optic cable was connected to a CCD spectrometer (Ocean Optics S-2000). Reflectivity spectra were recorded in the wavelength range of 400-1000 nm, with a spectral acquisition time of 0.1 s. A FFT using algorithm from WaveMetrics Inc. Igor program library was applied to the resulting spectra.

Preparation of the polymer fiber arrays and adhesion measurements. The silicon pore array templates were treated for 5 min with RF oxygen plasma (50 W) and silanized by immersing them into a mixture of 5 ml heptane (anhydrous 99%) with 5 ml of dichloromethane (anhydrous 99%) and 100 µl (heptadecafluoro-1,1,2,2-tetrahydrodecyl) dimethylchlorosilane at room temperature for 1 h. The samples were then washed in dichloromethane, dried with nitrogen and placed on a hot plate in air for 10 min at 100 ^{o}C. PDMS (Silgard 184, Dow Corning) precursor mixture (1:5 ratio of catalyst: base material) was casted on the silanized surfaces and allowed to cure for 8 h at 80 ^{o}C. For hot embossing experiments, the silicon template was placed on a hot plate (180 ^{o}C) with a PC foil (10 x 10 mm, 1 mm thick) in contact and pressed against the template using a 400 g weight. After cooling below Tg, the template was detached and ready for reuse. Adhesion measurements were performed with the previously described home-built adhesion tester MAD.[20] In short, the samples were placed on a moving stage consisting of a 6-axis table (Hexapod, Physik Instrumente Karlsruhe) for positioning and a 3 axis piezo (Nanocube, Physik Instrumente Karlsruhe) for displacement control. Forces were measured with a calibrated glass beam (spring constant of 138 N/m), which was fixed on both ends to ensure a parallel beam bending. A mirror was glued to the top of the cantilever and a borosilicate glass probe with a diameter of 4 mm (Goodfellow) was glued to the bottom. The cantilever displacement was measured with a laser interferometer (Miniatur Interferometer SP 120, SIOS Messtechnik GmbH), where the laser

beam was reflected on the mirror. Prior to adhesion measurements, the probe was thoroughly cleaned using ethanol and isopropanol. Afterwards, 1000 contacts were made on a smooth part of the sample to avoid transfer effects of non-crosslinked oligomers.[21] The sample was brought into contact with the probe, measuring the compressive force (preload), and retracted again, determining the tensile force (pull-off force). The measurement system was controlled and the data were collected by a program based on LabView (National Instruments). All adhesion measurements were performed with a displacement velocity of 5 μm/s. On each measurement position, the pull-off force was determined for various preloads (preload scan) and repeated 3 times. Adhesion was determined on 5 different positions of each sample as well as on 3 unpatterned positions of the respective sample that served as reference.

3. RESULTS AND DISCUSSION

Fabrication of submicron pore arrays. The process steps are schematically illustrated in Figure 1a-c. Gold thin films were deposited on a silicon wafer using a standard DC magnetron sputtering system. Convective assembly deposited a hexagonally close-packed PS monolayer on top (Figure 1d). Subsequent sputter etching process etched the PS spheres (thereby increasing interparticle spacing) and the exposed gold film (unmasked by the etched PS particles). Figures S1-S3 (Supporting Information) provide more details on the sputter etch step. The process yielded dense arrays of gold discs with sharp edges that inherited the long-range order of the self-assembled particle monolayer. Figure 1e shows the gold disc array after removing the PS particles. Figure S4 (Supporting Information) shows the dependency of the discs size with sputter etching time for different initial particle diameters. The resulting discs work surprisingly well for etching the silicon by MACE, without deviating from the vertical etching direction,

yielding ordered arrays of vertically aligned pores with uniform cross sections and spacing (Figure 1f). The pores faithfully retained the 2D geometric configuration of the gold discs. The center-to-center distance between pores is set by the diameter of the polymer particles. Figure 2a shows an array of pores (D~400 nm) achieved using PS particles with diameter of 500 nm. Typical cross-section morphology of the pore arrays is displayed in Figure 2b. The density of the pore array is tunable via sputter etching time that sets the packing density (from 0.29 to 0.82) of the discs used as catalysts in the MACE process (Figure 2c-e). The depth of the pores was easily adjusted by MACE time as shown in Figure 3. Aspect ratios up to 5 were possible (Figure 3d) while retaining the lateral geometry, despite thin walls separating the adjacent pores. Aspect ratios above 5 can be achieved with longer etching times. That can lead, however, to merging of either two or three pores at the base. A critical prerequisite to achieving dense arrays of deep vertically-aligned pores were the metal discs with smooth, well-defined edges. Compared to other results[1,22,23] our pore arrays are denser, with better profile of the pores (i.e. sharp edges with virtually no deviation from circular shape and with smooth vertical walls) of submicron diameters with aspect ratio above 5 – which is high considering the challenges of using isolated metal structures as opposed to the widely used perforated metal layers that yields silicon pillars or nanowires. The profile of our structures as well as the aspect ratio achievable with our method are attributed to the fabrication approach that is able to produce gold discs with sharp edges in uniform contact with the silicon surface. To the best of our knowledge, dense arrays of submicron pores with such aspect ratio fabricated by MACE have not been reported so far. After MACE, the gold discs remained at the base of the pores. They could be removed by short treatment in aqua regia or remain in place when their presence was desirable (e.g. sensor applications, vide infra).

Vertical pore arrays with long-range order are a ~~desirable~~ favorable configuration for a ~~multitude~~ variety of applications. Some of them were explored in this work, emphasized in the following.

Detection of small molecules via SALDI-MS. Matrix-assisted laser desorption/ionization (MALDI) – a soft ionization technique used in mass spectrometry (MS) – is an indispensable tool in macromolecule analysis. The detection of small molecules (MW < 500 Da) remains challenging, because the matrix produces fragment and adduct signals in the low-molecular-weight region that obscure the analytes' signals. Matrix-free detection as in surface-assisted laser desorption/ionization (SALDI) obviates this limit.[24] There is general consensus within the literature that the sensitivity of matrix free techniques is governed by factors including a high surface area and UV absorptivity.[25] In SALDI, inorganic nanostructured surfaces with suitable chemical functionalization absorb UV laser energy and transfer it to the adsorbed small molecular analytes, allowing effective small molecule detection with low background noise. Porous silicon prepared by electrochemical anodization of silicon wafers and functionalized with fluorosilanes has been one of the most successful SALDI surfaces so far.[24] Compared to other substrates with disordered pores, our pore arrays provide increased active areas together with excellent homogeneity of the packing. Here we employ the ordered pore arrays as SALDI substrates for sensitive detection of methadone. Methadone is a synthetic opioid drug that is used for the treatment of opioid dependency, for example in heroin addicts.[26] **Figure 4** displays representative SALDI mass spectra for methadone in water at 1000 ng/mL. The major peak observed at m/z 310 was attributed to the protonated mass of methadone. Low background noise and the generation of the molecular ion for methadone detectable at concentrations of 10 ng/ml that were reached without optimization demonstrate that our pore arrays can be used for highly sensitive direct detection of methadone drug molecules using SALDI-MS.

Enteric virus detection by electrochemical impedance spectroscopy (EIS). We were interested in low-cost biosensors that operate label-free with a small number of analysis steps,[27] suitable for portable point-of-care biomedical and environmental testing. Non-faradaic EIS is a highly sensitive label-free electrochemical technique that can be used to develop such kind of biosensors. It only allows the flow of transient currents without charge transfer, showing a capacitive behavior caused by the blockage of the electrode surface upon the binding event. There is a recent focus on exploiting the unique properties of nanostructured materials as electrochemical interfaces in sensors. The use of these structures involves different advantages that may vary depending on the sensing approach. Particularly interesting is the use of pores with different pore diameter/length ratio for sensing purposes based on measuring changes in electrical conductance due to pore blockage (inspired by natural channels).[28] Electrochemical sensing using pores usually provides higher sensitivity than flat electrodes. Furthermore, the pore arrays can be easily combined with label-free sensing strategies, resulting in rapid and simple measurements. Apart from performing as sensing platforms, the pore arrays can be employed to analyse complex matrixes due to their performance as filters, minimizing matrix interferences based on size-exclusion effects. Anodised aluminum oxide, as solid-state nanopore arrays, has been used for electroanalytical purposes. Nevertheless, our pore arrays offer additional advantages due to the uniformity of the pores that have well-defined profile and straight walls. The pore arrays' morphological features can be easily tailored to maximize the pores blockage upon binding of a target analyte to the functionalized surface, which would result in improved sensitivity. For our experiments, a dense array of pores acted as nanowells in which the biorecognition event took place. The gold discs at the bottom of the pores were functionalized with mercaptopropionic acid, and polyclonal anti-MS2 antibodies were affixed by carbodiimide

coupling. The MS2 bacteriophage virus, a surrogate for pathogenic enteric viruses and also an indicator of fecal bacteria contamination in drinking water, was then detected by non-faradaic EIS.[5,29,30] **Figure 5a** shows that the antibody-modified pore array decreased in capacitance (C) as the phage concentration increased, whereas the negative control substrate functionalized with BSA did not change. Changes in capacitance were due to the displacement of water and ions from the surface by the phage, the increase in thickness and decrease in relative dielectric constant (ε_r) of the receptor layer, or combinations thereof. The charge-transfer resistance (R_{ct}) increased with increasing concentration of MS2 bacteriophage (**Figure 5b**). Even though capacitance is the preferred circuit element to monitor affinity binding in non-faradaic EIS, both capacitance and R_{ct} are dependent on the MS2 concentration. The detection limit determined as 3σ/sensitivity is equal to 0.9 pfu/mL or 1.5 pfu/mL using capacitance or Rct, respectively, where σ is the standard deviation for the blank (PBS solution without MS2). Our biosensor is capable of detecting MS2 virus at concentrations at least five orders of magnitude better than current MS2 assays.[31,32,33] Our experiments prove that such pore arrays can be employed as biosensors, providing a versatile platform in terms of fabrication and functionalization, which could be easily tailored to a wide range of analytes of interest.

Enzyme nanoreactors. The specificity and sensitivity of biosensor can often be increased when coupling it to enzymatic reactions. Pico- to femtolitre reactions vessels have been created using lab-on-chip technologies;[34] they were capable of single molecule detection[35] and massively parallel DNA sequencing.[36] For example, the ability to "dial in" the physical properties of the effective pore size and thus the total volume of each pore, both reduces the requested sample volume and allows for rapid analysis of enzyme activity. Our dense array in Si offer further benefits, including pore walls robustness which assists in maintaining the nanoreactor volume

constant, as well as stability to various reaction solvents. The direct immobilization of large biomolecules on the gold disc within the pore is less cumbersome than other immobilization strategies, such as enzyme entrapment, and physical adsorption. Via direct enzymes attachment to a solid substrate, the vertical pores array offer improved enzyme stability. We demonstrated the principle by immobilizing horseradish peroxidase (HRP) onto the gold discs at the base of the pores, and following the catalytic activity of roughly 10,000 to 50,000 HRP enzymes within each pore (here with volumes of ~8,5 fL) upon incubation with a fluorogenic substrate (Figure 6). Using a simple fluorescence microscope, we could follow parallel reactions within the pores. The density of the array therefore made it possible to image and analyze a large number (>150) of reactions in a single optical micrograph.

Anti-reflective and interferometric properties. Pores change the optical reflectivity of silicon. Surface texturing can reduce reflectance to approximately 10% in mono-crystalline silicon.[37] Anti-reflection surfaces are used in lenses, eye-glasses, windshield screens, mirrors, diode lasers, and solar cells.[38,39] Submicron pores are antireflective and concave, which makes them inherently more robust than nanowires and other convex structures. Our fabrication strategy enables fine control over the geometry of the vertical pore arrays, and consequently control over anti-reflective and interferometric properties. In particular, tuning of the pore aspect ratio leads to a significant reflection reduction over broad spectral regime. As such, the array features excellent anti-reflective properties that could be potentially employed in anti-reflection surfaces. Optical reflectometry measurements on our ordered pore arrays reveal absolute reflectance of approximately 12.6% for 2.6 μm diameter pores with an aspect ratio of Γ~1.8 and 3% for 230 nm diameter pores with Γ~25 (Figure 7). The reduction was comparable or greater

than that reported for porous silicon pyramids,[40,41] other (less dense) pore arrays,[42,43,44] and vertically aligned SiNW arrays.[2,45,46,47]

Interestingly, thin pore arrays also exhibit optical interference when illuminated with light in a wavelength range close to pore diameter. The interference depends on the refractive index of the medium in the pores, an effect that is commonly exploited for interferometric biosensing.[48,49] Interference fringes occur at wavelengths λ depending on the pore length and are described by the Fabry-Pérot relationship $m\lambda = 2nL$, where m is an integer corresponding to the spectral order of the fringe, n the refractive index of the medium inside the pore and L the pore length. Figure 8 shows how the silicon pore arrays were examined with respect to refractive index unit (RIU) sensitivity. The value of the effective optical thickness (EOT) (2nL) was obtained from the position of the peak in the Fourier transform in response to solvent infiltration into the pores and compared to anodized porous silicon.[50,51,52] The sensitivity value was calculated from the slope of a linear least squared line fit from the plot of % EOT shift vs. refractive index unit (RIU) and was found to be 17.6% RIU^{-1}, only slightly lower than for anodized porous silicon with disordered pores and large pore size dispersity (18-20% RIU^{-1}).[52,53] Interferometric sensors could benefit from uniform pores that only detect species which fit into the pores.[54,55] In addition, anodized porous silicon is susceptible to oxidative hydrolysis in aqueous medium whilst our arrays are stable under these conditions.[56]

Polymer fiber arrays by replica molding. Surface microstructures can tune the adhesive properties of polymer surfaces. Bioinspired, artificial systems range from highly adhesive surfaces (e.g. gecko-inspired structures)[57,58] to anti-adhesive surfaces (e.g. moth-eye anti-dust structures).[59] We used our submicron pore arrays in silicon to mould the elastomer PDMS (Sylgard 184), which has a bulk modulus of approximately 2.1 MPa. A dense array of

sufficiently thin fibres should decrease the effective Young's modulus to values below 100 kPa, the maximum effective modulus for tackiness according to the Dahlquist criterion.[60] The surface should become tacky. At the other extreme, we prepared non-adhesive moth-eye inspired surfaces from polycarbonate (PC), which has a bulk modulus of approximately 2.2 GPa. Dense fibre arrays reduce adhesion of stiff materials by minimizing the contact area and introducing defects. Figure 9 summarizes the replication process. First, the pore arrays were coated with a hydrophobic fluorosilane self-assembled monolayer (SAM) to decrease surface energy. PDMS precursor mixture was casted onto the templates and cured. The peeled off PDMS retained a dense forest of pillars as shown in Figure 9d. The silicon templates could be reused several times without noticeable degradation. The stiffer PC was moulded by bringing it into contact with the fluorinated pores, heating to above glass transition and applying pressure (Figure 9e).

Adhesion measurements on the polymer fiber arrays. Figure S5a shows pull-off forces as a function of preload for a representative set of measurements on PDMS samples. Red circles indicate a smooth PDMS reference sample. The pull-off forces for nanofibrous PDMS surfaces exhibited large variation for the different testing positions. With one exception (position 5), all observed pull-off forces were lower than on flat PDMS. Figure 9d shows an SEM micrograph that explains this unexpected result: the submicron PDMS structures have collapsed and form larger accumulations of pillars, which obliviates any adhesion-enhancing effect.[58] The collapse of the structures is unexpected, because larger (microscale) PDMS pillars with aspect ratio of 5 and higher do not collapse.[61] We suggest that the mechanical properties of submicron PDMS structures deviate from bulk properties, as previously found for thin PDMS membranes.[62] The limiting factor for the application as bioinspired adhesive at submicron scales are the mechanical properties of PDMS rather than the patterning method. Figure S5b documents adhesion

measurements on the moth-eye inspired anti-adhesive PC surfaces displayed in Figure 9e. Red circles show the adhesion of the smooth reference sample. The adhesion of all patterned PC samples is very low and reaches the limits of the adhesion measurement. Compared to the reference sample, the adhesion is reduced by a factor of ~40. Such surfaces are suitable as adhesion-preventing coating.

4. CONCLUSION

In summary, we introduced a particle-based method to create dense arrays of straight, submicron pores in silicon that can be used for applications that require high void fraction and uniform geometries. Arrays of gold discs prepared via self-assembly and sputter etching were used as catalysts in a MACE process to achieve well-defined pores in silicon. The pores were exceptionally straight with smooth walls and flat bottoms that still contained gold discs. The array spacing, the pore diameter and depth could be tuned over a wide range via particle size, sputter etching and MACE processing times, respectively. We applied the pore arrays as platforms for surface-assisted laser desorption/ionization (SALDI) mass spectrometry (MS), as electrochemical and optical biosensors and for enzyme nanoreactors. They also possess excellent anti-reflective properties. When used for replica molding, the silicon templates yielded fibre arrays of polydimethylsiloxane (PDMS) and polycarbonate (PC) with exceptional density, suitable for surfaces with controlled adhesion. Many other applications are expected to profit from the pore arrays discussed here.

AUTHOR INFORMATION

Corresponding Authors

*tobias.kraus@inm-gmbh.de,

*nico.voelcker@unisa.edu.au

Author Contributions

D.B. and R.E. contributed equally to this work.

Notes

The authors declare no competing financial interest.

ACKNOWLEDGMENT

We thank Prof. E. Arzt for stimulating discussions and for his continuing support of the project. We gratefully acknowledge funding from the German Science Foundation (DFG), in the framework of Priority Programme 1420. Funding from the Australia–Germany Researcher Mobility Programme and the DAAD-ATN travel grant scheme is also acknowledged.

ASSOCIATED CONTENT

Supporting Information Available: The file contains additional details pertaining to the fabrication of gold disc arrays as well as adhesion measurements performed on the polymer fiber arrays..

This material is available free of charge via the Internet at http://pubs.acs.org.

REFERENCES

1. Peng, K.-Q.; Wang, X.; Li, L.; Wu, X.-L.; Lee, S.-T. High-Performance Silicon Nanohole Solar Cells. *J. Am. Chem. Soc*. **2010,** *132*, 6872-6873.
2. Li, X. Metal Assisted Chemical Etching for High Aspect Ratio Nanostructures: A Review of Characteristics and Applications in Photovoltaics. *Curr. Opin. Solid State Mater. Sci.* **2012,** *16*, 71-81.
3. Gowda, S. R.; Pushparaj, V.; Herle, S.; Girishkumar, G.;Gordon, J. G.; Gullapalli, H.; Zhan, X.; Ajayan, P. M.; Reddy, A. L. M. Three-Dimensionally Engineered Porous Silicon Electrodes for Li Ion Batteries. *Nano Lett.* **2012,** *12*, 6060−6065.
4. Ge, M.; Fang, X.; Rong, J.; Zhou, C. Review of Porous Silicon Preparation and its Application for Lithium-ion Battery Anodes. *Nanotechnology* **2013,** *24*, 422001.
5. Vamvakaki, V.; Chaniotakis, N. A. DNA Stabilization and Hybridization Detection on Porous Silicon Surface by EIS and Total Reflection FT-IR Spectroscopy. *Electroanalysis* **2008,** *20*, 1845 - 1850.
6. Fu, J.; Wang, Y.-K.; Yang, M. T.; Desai, R. A.; Yu, X.; Liu, Z.; Chen, C. S. Mechanical Regulation of Cell Function with Geometrically Modulated Elastomeric Substrates. *Nature Methods* **2010,** *7*, 733 - 736.
7. Buzzi, S.; Robin, F.; Callegari, V.; Löffler, J. F. Metal Direct Nanoimprinting for Photonics. *Microelectron. Eng.* **2008,** *85*, 419-424.
8. Yang, M. T.; Sniadecki, N. J.; Chen, C. S. Geometric Considerations of Micro- to Nanoscale Elastomeric Post Arrays to Study Cellular Traction Forces. *Adv. Mater.* **2007,** *19*, 3119-3123.
9. Du Roure, O.; Saez, A.; Buguin, A.; Austin, R. H.; Chavrier, P.; Silberzan, P.; Ladoux, B. Force Mapping in Epithelial Cell Migration. *Proc. Natl. Acad. Sci. U. S. A.* **2005,** *102*, 2390–2395.
10. Byeon, K.-J.; Hwang, S.-Y.; Lee, H. Fabrication of Nano-hole Array Patterns on Transparent Conducting Oxide Layer using Thermally Curable Nanoimprint Lithography. *Microelectron. Eng.* **2008,** *85*, 830-833.
11. Plettl, A.; Enderle, F.; Saitner, M.; Manzke, A.; Pfahler, C.; Wiedemann, S.; Ziemann, P. Non-Close-Packed Crystals from Self-Assembled Polystyrene Spheres by Isotropic Plasma Etching- Adding Flexibility to Colloidal Lithography. *Adv. Funct. Mater.* **2009,** *19*, 3279–3284.
12. Shiao, M.-H.; Chang, C.-M.; Huang, S.-W.; Lee, C.-T.; Wu, T.-C.; Hsueh, W.-J.; Ma, K.-J.; Chiang, D. The Sub-Micron Hole Array in Sapphire Produced by Inductively-Coupled Plasma Reactive Ion Etching. *J. Nanosci. Nanotechnol.* **2012,** *12*, 1641-1644.
13. Mai, T. T.; Lai, C. Q.; Zheng, H.; Balasubramanian, K.; Leong, K. C.; Lee, P. S.; Lee, C.; Choi, W. K. Dynamics of Wicking in Silicon Nanopillars Fabricated with Interference Lithography and Metal-Assisted Chemical Etching. *Langmuir* **2012,** *28*, 11465−11471.
14. Luo, M.; Epps, T. H. Directed Block Copolymer Thin Film Self-Assembly: Emerging Trends in Nanopattern Fabrication. *Macromolecules* **2013,** *46*, 7567-7579.
15. Huang, Z.; Geyer, N.; Werner, P.; De Boor, J.; Gösele, U. Metal-Assisted Chemical Etching of Silicon: A Review. *Adv. Mater.* **2011,** *23*, 285-308.
16. Huang, Z; Fang, H.; Zhu, J. Fabrication of Silicon Nanowire Arrays with Controlled Diameter, Length, and Density. *Adv. Mater.* **2007,** *19*, 744-748.

17. Huang, Z.; Shimizu, T.; Senz, S.; Zhang, Z.; Zhang, X; Lee, W.; Geyer, N.; Gösele, U. Ordered Arrays of Vertically Aligned [110] Silicon Nanowires by Suppressing the Crystallographically Preferred <100> Etching Directions. *Nano Lett.* **2009,** *9*, 2519–2525.
18. Brodoceanu, D.; Fang, C.; Voelcker, N. H.; Bauer. C. T.; Wonn, A.; Kroner, E.; Arzt, E.; Kraus, T. Fabrication of Metal Nanoparticle Arrays by Controlled Decomposition of Polymer Particles. *Nanotechnology* **2013,** *24*, 085304.
19. Prevo, B. G.; Velev, O. D. Controlled, Rapid Deposition of Structured Coatings from Micro- and Nanoparticle Suspensions. *Langmuir* **2004,** *20*, 2099-2107.
20. Kroner, E.; Blau, J.; Arzt, E. Note: An Adhesion Measurement Setup for Bioinspired Fibrillar Surfaces using Flat Probes. *Rev. Sci. Instrum.* **2012,** *83*, 016101.
21. Kroner, E.; Maboudian, R.; Arzt, E. Adhesion Characteristics of PDMS Surfaces During Repeated Pull-off Force Measurements. *Adv. Eng. Mater.* **2010,** *12*, 398 - 404.
22 Vlad, A.; Frölich, A; Zebrowski, T.; Dutu, C. A.; Busch, K.; Melinte, S.; Wegener, M.; Huynen, I. Direct Transcription of Two-Dimensional Colloidal Crystal Arrays into Three-Dimensional Photonic Crystals. *Adv. Funct. Mater.* **2013**. *23*, 1164–1171.
23 Asoh, H.; Arai, F.; Ono, S. Effect of noble metal catalyst species on the morphology of macroporous silicon formed by metal-assisted chemical etching. *Electrochimica Acta* **2009**, *54*, 5142–5148.
24. Arakawa, R.; Kawasaki, H. Functionalized Nanoparticles and Nanostructured Surfaces for Surface-Assisted Laser Desorption/Ionization Mass Spectrometry. *Anal Sci* **2010,** *26*, 1229-1240.
25 Wei, J.; Buriak, J. M.; Siuzdak, G. Desorption–ionization mass spectrometry on porous silicon. *Letters to Nature* **1999**, *399*, 243-246.
26. Strain, E. C.; Bigelow, G. E.; Liebson, I. A.; Stitzer, M. L. Moderate- vs High-Dose Methadone in the Treatment of Opioid Dependence A Randomized Trial. *JAMA, J. Am. Med. Assoc.* **1999,** *281*, 1000-1005.
27. Prodromidis, M. I. Impedimetric Immunosensors—A Review. *Electrochim. Acta* **2010,** *55* (14), 4227-4233.
28 Muñiz, A. E.; Merkoçi, A. Nanochannels Preparation and Application in Biosensing. *ACS Nano* **2012**, *6*, 7556-7583.
29. Nagaraj, V. J.; Jacobs, M.; Vattipalli, K. M.; Annam, V. P.; Prasad, S. Nanochannel-Based Electrochemical Sensor for the Detection of Pharmaceutical Contaminants in Water. *Environ. Sci.: Processes Impacts* **2014,** *16*, 135-140.
30. Prasad, S.; Selvam, A. P.; Reddy, R. K.; Love, A. Silicon Nanosensor for Diagnosis of Cardiovascular Proteomic Markers *J. Lab. Autom.* **2012,** *18*, 143-151.
31. Rao RS; Visuri SR; McBride MT; Albala JS; Matthews DL; Coleman, M. A. Comparison of Multiplexed Techniques for Detection of Bacterial and Viral Proteins. *J Proteome Res.* **2004,** *3*, 736-742.
32. Rossi, A. M.; Wang, L.; Reipa, V.; Murphy, T. E. Porous Silicon Biosensor for Detection of Viruses. *Biosens Bioelectron.* **2007,** *23*, 741-745.
33. Usachev, E. V.; Tam, A. M.; Usacheva, O. V.; Agranovski, I. E. The Sensitivity of Surface Plasmon Resonance Based Viral Aerosol Detection. *J. Aerosol Sci.* **2014,** *76*, 39-47.
34. Margulies M.; Egholm, M; Altman, W. E.; Attiya, S.; Bader, J. S.; Bemben, L. A.; Berka, J.; Braverman, M. S.; Chen, Yi.-Ju; Chen, Z.; Dewell, S. B; Du, L.; Fierro, J. M.; Gomes, X. V.; Godwin, B. C.; He, W.; Helgesen, S.; Ho, C. H.; Irzyk, G.P.; Jando, S.C.; Alenquer, M.L.I.; Jarvie, T.P.; Jirage, K. B.; Kim, J.-B.; Knight, J. R.; Lanza, J. R.; Leamon, J. H.; Lefkowitz, S.

M.; Lei, M.; Li, J.; Lohman, K. L.; Lu, H.; Makhijani, V. B.; McDade, K. E.; McKenna, M. P.; Myers, E. W.; Nickerson, E.; Nobile, J. R.; Plant, R.; Puc, B. P.; Ronan, M. T.; Roth, G. T.; Sarkis, G. J.; Simons, J. F.; Simpson, J. W.; Srinivasan, M.; Tartaro, K. R.; Tomasz, A.; Vogt, K. A.; Volkmer, G. A.; Wang, S. H.; Wang, Y.; Weiner, M. P.; Yu, P.; Begley R. F.; Rothberg, J. M. Genome Sequencing in Open Microfabricated High Density Picoliter Reactors. *Nature* **2005,** *437*, 376–380.
35. Craighead, H. Future Lab-on-a-Chip Technologies for Interrogating Individual Molecules. *Nature* **2006,** *442*, 387-393.
36. Rothberg, J. M.; Hinz, W.; Rearick, T.M.; Schultz, J.; Mileski, W.; Davey, M.; Leamon, J. H.; Johnson, K.; Milgrew, M. J.; Edwards, M.; Hoon, J.; Simons, J. F.; Marran, D,; Myers, J. W.; Davidson, J. F.; Branting, A.; Nobile, J. R.; Puc, B. P.; Light, D.; Clark, T. A.; Huber, M.; Branciforte, J. T.; Stoner, I. B.; Cawley, S. E.; Lyons, M.; Fu, Y.; Homer, N.; Sedova, M.; Miao, X.; Reed, B.; Sabina, J.; Feierstein, E.; Schorn, M.; Alanjary, M.; Dimalanta, E.; Dressman, D.; Kasinskas, R.; Sokolsky, T.; Fidanza, J. A.; Namsaraev, E.; McKernan, K. J.; Williams, A.; Roth, G. T.; Bustillo, J. An Integrated Semiconductor Device Enabling Non-Optical Genome Sequencing. *Nature* **2011,** *475*, 348-352.
37. Geng, X.; Qi, Z.; Li, M.; Duan, B. K.; Zhao, L.; Bohn, P. W. Fabrication of Antireflective Layers on Silicon using Metal-Assisted Chemical Etching with In Situ Deposition of Silver Nanoparticle Catalysts. *Sol. Energy Mater. Sol. Cells* **2012,** *103*, 98-107.
38. Ye, X.; Qi, L. Two-Dimensionally Patterned Nanostructures Based on Monolayer Colloidal Crystals: Controllable Fabrication, Assembly, and Applications. *Nano Today* **2011,** *6*, 608-631.
39. Raut, H. K.; Ganesh, V. A.; Nair, A. S.; Ramakrishna, S. Anti-reflective Coatings: A Critical, In-Depth Review. *Energy Environ. Sci.* **2011,** *4*, 3779-3804.
40. Li, R.; Wang, S.; Chuwongin, S.; Weidong, Z. Nanoscale Silver-Assisted Wet Etching of Crystalline Silicon for Anti-Reflection Surface Textures. *J. Nanosci. Nanotechnol.* **2013,** *13*, 493-497.
41. Xiao, J.; Wang, L.; Li, X.; Pi, X.; Yang, D. Reflectivity of Porous-Pyramids Structured Silicon Surface. *Appl. Surf. Sci.* **2010,** *257*, 472–475.
42. Huang, M.-J.; Yang, C.-R; Chiou, Y.-C.; Lee, R.-T. Fabrication of Nanoporous Antireflection Surfaces on Silicon. *Sol. Energy Mater. Sol. Cells* **2008,** *92*, 1352-1357.
43. Lee, M.-H.; Khang, D.-Y. Facile Generation of Surface Structures having Opposite Tone in Metal-Assisted Chemical Etching of Si: Pillars vs. Holes. *RSC Adv.* **2013,** *3*, 26313-26320.
44. Ji, J.; Zhang, H.; Qiu, Y.; Wang, L.; Wang, Y.; Hu, L. Fabrication and Photoelectrochemical Properties of Ordered Si Nanohole Arrays. *Appl. Surf. Sci.* **2014,** *292*, 86-92.
45. Chang, H.-C.; Lai, K.-Y.; Dai, Y.-A.; Wang, H.-H.; Lin, C.-A.; He, J.-H. Nanowire Arrays with Controlled Structure Profiles for Maximizing Optical Collection Efficiency. *Energy Environ. Sci.* **2011,** *4*, 2863-2869.
46. Wang, H.-P.; Lai, K.-Y.; Lin, Y.-R.; Lin, C.-A.; He, J.-H. Periodic Si Nanopillar Arrays Fabricated by Colloidal Lithography and Catalytic Etching for Broadband and Omnidirectional Elimination of Fresnel Reflection. *Langmuir* **2010,** *26*, 12855-12858.
47. Xie, W. Q.; Oh, J. I.; Shen, W. Z. Realization of Effective Light Trapping and Omnidirectional Antireflection in Smooth Surface Silicon Nanowire Arrays. *Nanotechnology* **2011,** *22*, 065704.

48. Lin, V. S.-Y.; Motesharei, K.; Dancil, K.-P. S.; Sailor, M. J.; Ghadiri, M. R. A Porous Silicon-Based Optical Interferometric Biosensor. *Science* **1997,** *278*, 840-843.
49. Janshoff, A.; Dancil, K.-P. S.; Steinem, C.; Greiner, D. P.; Lin, V. S.-Y.; Gurtner, C.; Motesharei, K.; Sailor, M. J.; Ghadiri, M. R. Macroporous p-Type Silicon Fabry−Perot Layers. Fabrication, Characterization, and Applications in Biosensing. *J. Am. Chem. Soc.* **1998,** *120*, 12108 -12116.
50. Min, H.-K.; Yang, H.-S.; Cho, S. M. Extremely Sensitive Optical Sensing of Ethanol using Porous Silicon. *Sens. Actuators, B* **2000,** *67*, 199-202.
51. Gaburro, Z.; Daldosso, N.; Pavesi, L.; Faglia, G.; Baratto, C.; Sberveglieri, G. Monitoring Penetration of Ethanol in a Porous Silicon Microcavity by Photoluminescence Interferometry. *Appl. Phys. Lett.* **2001,** *78*, 3744-3746.
52. Dronov, R.; Jane, A.; Shapter, J. G.; Hodges, A.; Voelcker, N. H. Nanoporous Alumina-Based Interferometric Transducers Ennobled. *Nanoscale* **2011,** *3*, 3109-3114.
53. Volk, J.; Le Grand, T.; Bársony, I.; Gombkötő, J.; Ramsden, J. J. Porous Silicon Multilayer Stack for Sensitive Refractive Index Determination of Pure Solvents. *J. Phys. D: Appl. Phys.* **2005,** *38*, 1313-1317.
54. Jane, A.; Dronov, R.; Hodges, A.; Voelcker, N. H. Porous Silicon Biosensors on the Advance. *Trends Biotechnol.* **2009,** *27*, 230–239.
55. Anglin, E. J.; Cheng, L.; Freeman, W. R.; Sailor, M. J. Porous Silicon in Drug Delivery Devices and Materials. *Adv. Drug Delivery Rev.* **2008,** *60*, 1266-1277.
56. Pacholski, C.; Sartor, M.; Sailor, M. J.; Cunin, F.; Miskelly, G. M. Biosensing Using Porous Silicon Double-Layer Interferometers: Reflective Interferometric Fourier Transform Spectroscopy. *J. Am. Chem. Soc.* **2005,** *127*, 11636–11645.
57. Campo, A.; Greiner, C.; Arzt, E. Contact Shape Controls Adhesion of Bioinspired Fibrillar Surfaces. *Langmuir* **2007,** *23*, 10235-10243.
58. Kamperman, M.; Kroner, E.; Campo, A.; McMeeking, R. M.; Arzt, E. Functional Adhesive Surfaces with “Gecko” Effect: The Concept of Contact Splitting. *Adv. Eng. Mater.* **2010,** *12*, 335-348.
59. Peisker, H.; Gorb, S. N. Always on the Bright Side of Life: Anti-Adhesive Properties of Insect Ommatidia Grating. *J. Exp. Biol.* **2010,** *213*, 3457-3462.
60. Dahlquist, C. A. *Pressue-Sensitive Adhesives*; Marcel Dekker: New York, 1969.
61. Greiner, C. Size and Shape Effects in Bioinspired Fibrillar Adhesives, Ph.D. Thesis, University of Stuttgart, Stuttgart, Germany, 2007.
62. Liu, M.; Sun, J.; Sun, Y.; Bock, C.; Chen, Q. Thickness-Dependent Mechanical Properties of Polydimethylsiloxane Membranes. *J. Micromech. Microeng.* **2009,** *19*, 035028.

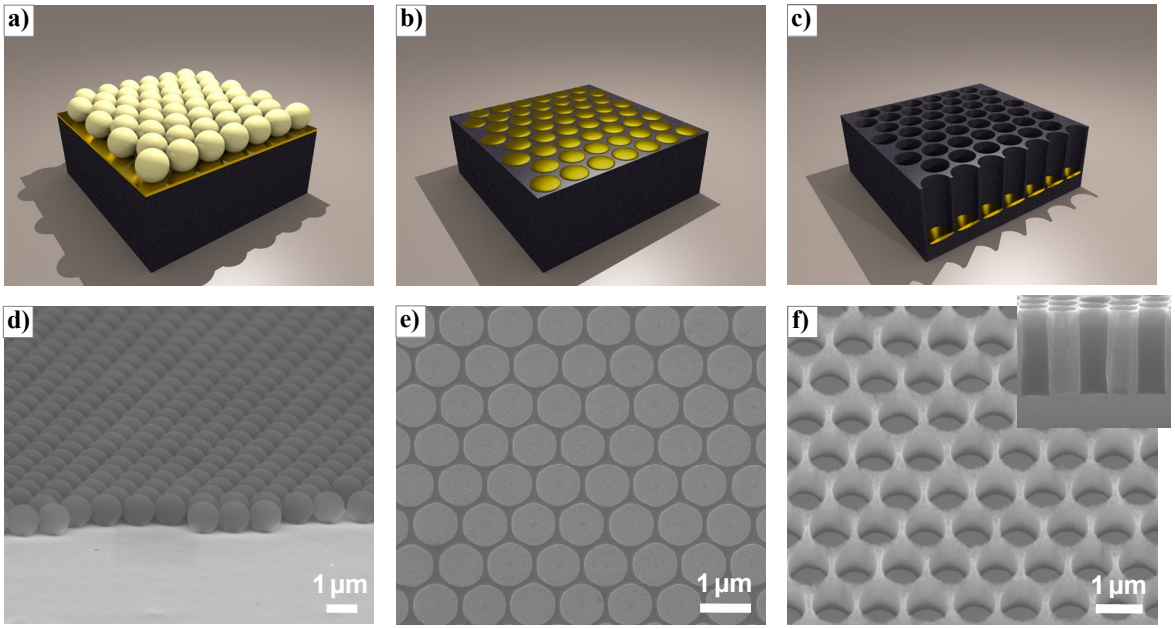

Figure 1. Pore array fabrication process. **a)** Schematic illustration of hexagonally close-packed polystyrene monolayer convectively assembled on a gold-coated silicon wafer. **b)** Schematic illustration of metal disc array after sputter etching process and subsequent removal of the remaining PS particles. **c)** Schematic view of dense array of pores etched into silicon via MACE using gold disc array as catalysts. **d-f)** SEM micrographs of the corresponding steps. The inset in (f) reveals the typical cross-section profile of the pores.

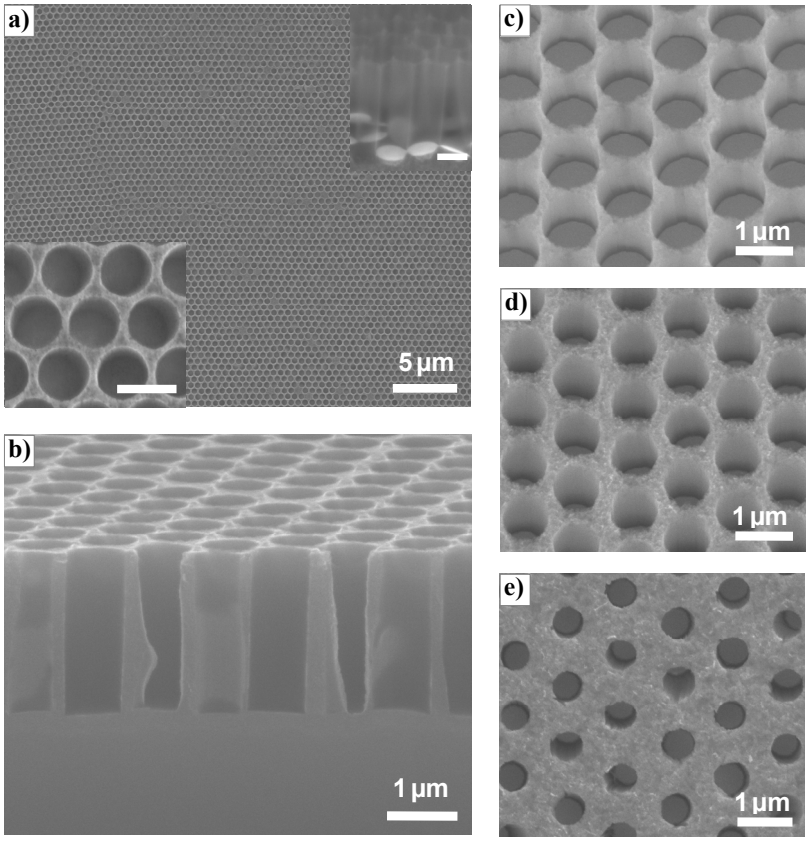

Figure 2. Pore arrays fabricated in silicon using different process parameters. **a)** SEM micrographs of an array of pores (D~400 nm) obtained using PS particles (D=500 nm). The bottom-left inset shows a close-up look (top view), while the top-right inset reveals the cross section with the gold discs visible at the bottom of the pores. The insets scale bars are 500 nm. **b)** Typical SEM cross section image of the pores array in silicon achieved using PS particles (D=1µm). The right side of the figure displays pore arrays with tuned density, achieved with gold discs of diameters defined at different sputter etching times: **c)** 40 s **d)** 65 s **e)** 75 s. The DC plasma discharge current was set to 20 mA during sputter etching process.

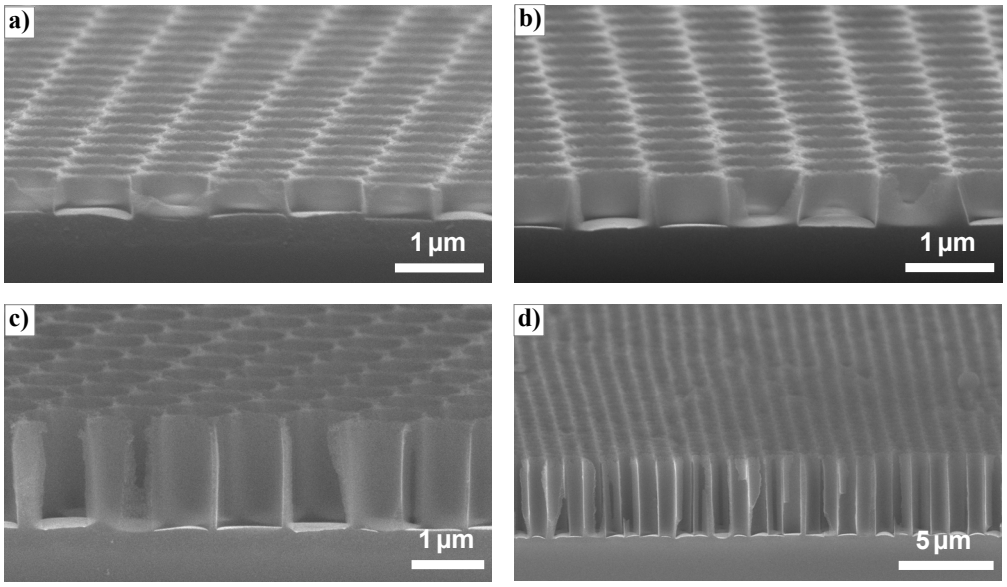

Figure 3. SEM micrographs of array of pores with submicron diameters (D~850 nm) fabricated in silicon at different MACE processing times: **a)** 2 min: Depth ~430 nm **b)** 4 min: Depth ~ 630 nm **c)** 10 min: Depth ~ 1.8 µm and **d)** 28 min: Depth ~ 4.5 µm (aspect ratio of about 5.3).

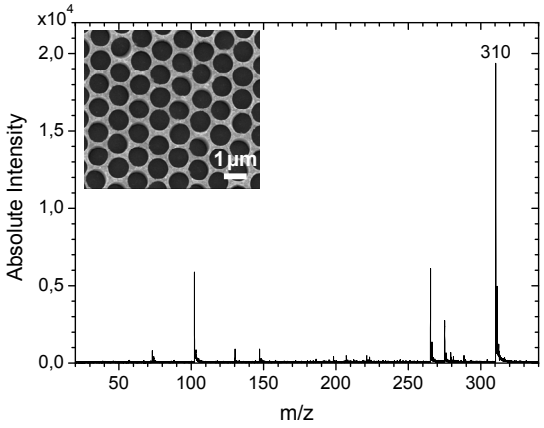

Figure 4. Representative SALDI mass spectrum for methadone with a MH^+ 310 peak obtained at a concentration of 1000 ng/mL. Inset: Pore array in silicon fabricated via MACE. Gold discs have been removed.

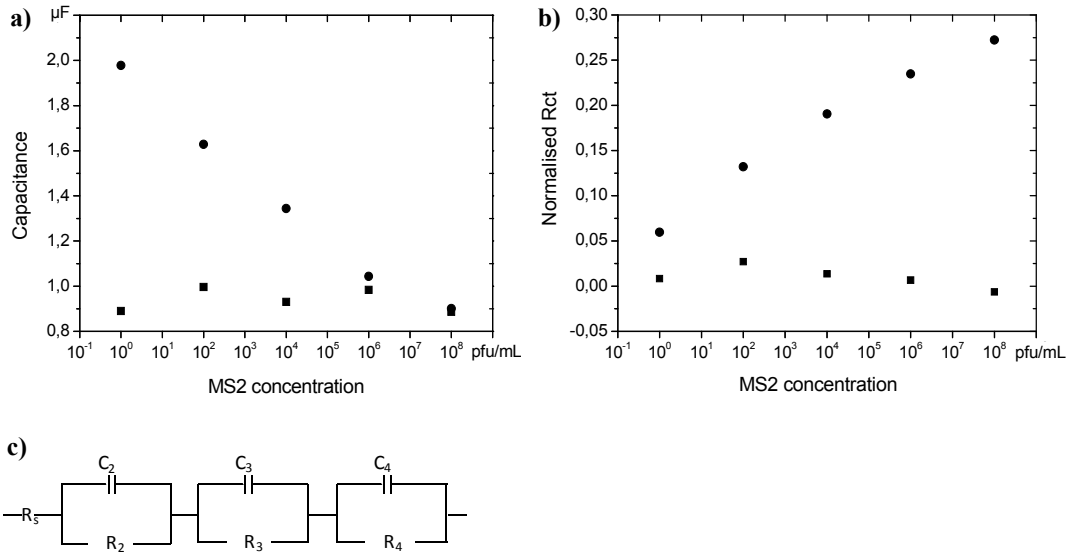

Figure 5. Bacteriophage detection by EIS. **a)** Plots of capacitance; **b)** Plots of normalized charge-transfer resistance $(R_{ct}^{f}-R_{ct}^{0})/R_{ct}^{0}$ values as a function of MS2 bacteriophage concentration obtained by using substrates modified with MS2-specific antibodies (circle) and BSA (square); **c)** Equivalent circuit model with three capacitors in series.

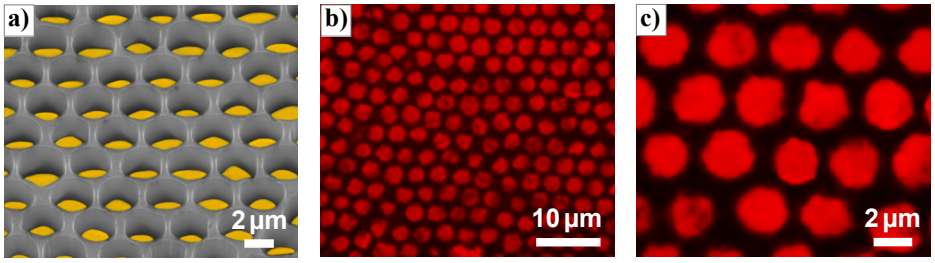

Figure 6. Massively parallel enzymatic reactions using silicon pore arrays. Resorufin synthesis is detected in each pore "nanoreactor" in real time by fluorescence microscopy. **a)** SEM image of the pore array with the gold discs (false-colored in yellow) at the base of the pores. HRP was immobilized on the gold discs within each nanoreactor pore. A substrate, Ampliflu, was enzymatically converted into the fluorescence dye Resorufin in the presence of H_2O_2 inside the nanoreactors. **b)** The array was observed by inverted fluorescence microscopy, allowing real time detection of the enzymatic reaction. **c)** Zoom-in showing individual pores with similar fluorescent intensity.

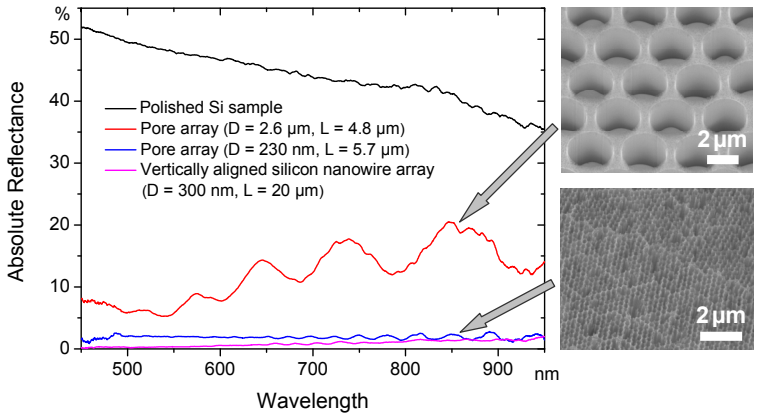

Figure 7. Plots of absolute reflectance as a function of wavelength recorded on two different ordered silicon pore arrays and compared to original polished silicon wafer and vertically aligned silicon nanowire arrays. Insets: SEM images of silicon pore arrays used for the reflectivity measurements (top: D=2.6 µm, L=4.8 µm; bottom: D=230 nm, L=5.7 µm).

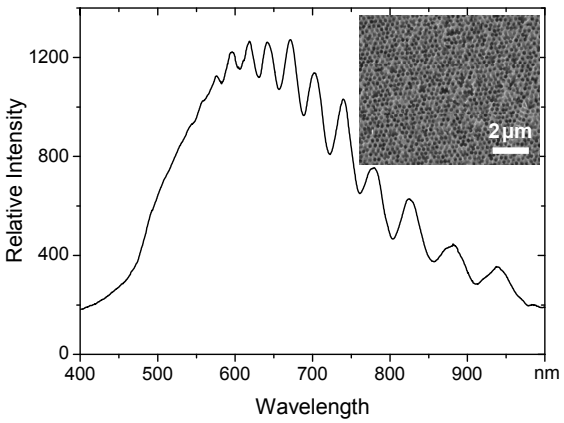

Figure 8. Interference fringe pattern of a dense pore array. The inset shows the silicon sample (pores diameters ~ 230 nm, depth ~ 1.8 µm) after etching the gold discs.

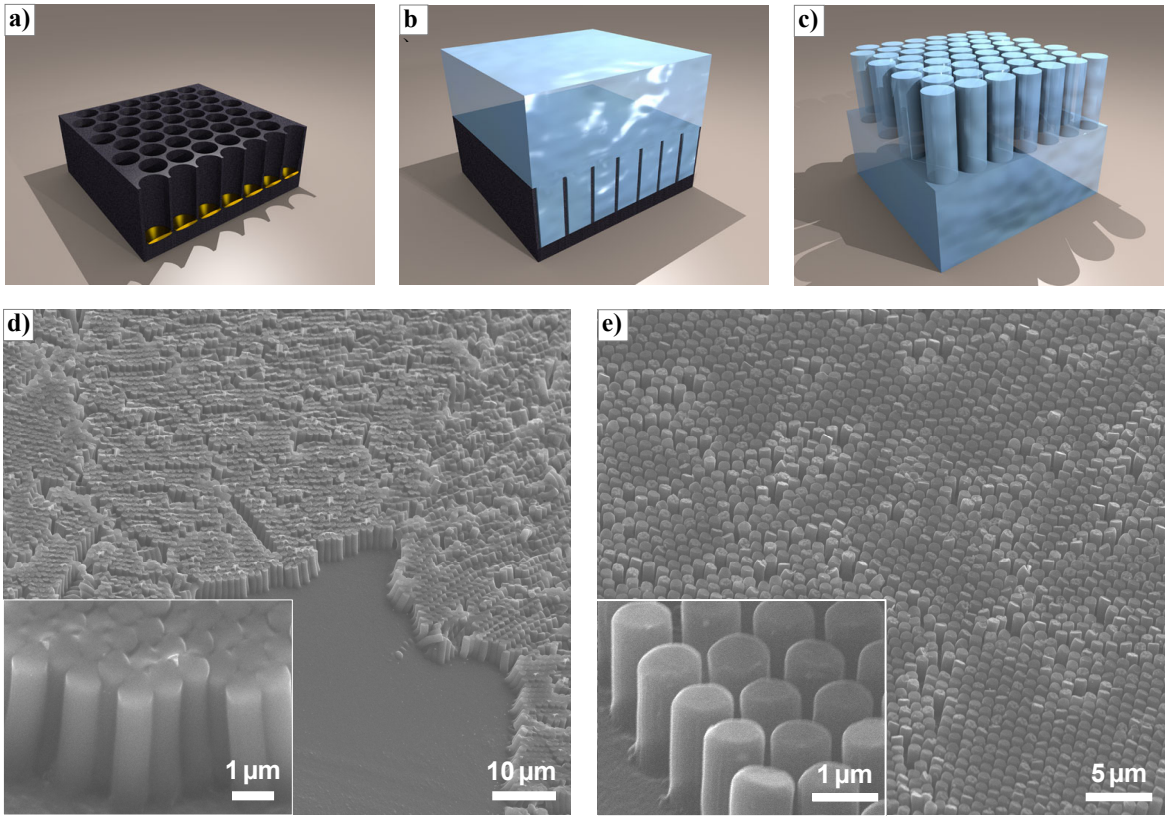

Figure 9. Fabrication of the polymer fiber arrays **a)** Schematic view of dense array of straight pores with flat bottom etched into silicon. **b)** Schematic illustration of polymer molding using silicon template. **c)** Schematic illustration of resulted pillar array structure. **d)** SEM micrograph of cured PDMS surface after replica molding sequence (casting/curing/peeling). **e)** SEM micrograph of microstructured PC surface achieved via hot embossing.

Table of Contents Graphic: